

# Conformational Changes in Nitric Oxide Synthases Induced by Chlorzoxazone and Nitroindazoles: Crystallographic and Computational Analyses of Inhibitor Potency<sup>†</sup>

Robin J. Rosenfeld,<sup>‡</sup> Elsa D. Garcin,<sup>‡</sup> Koustubh Panda,<sup>§</sup> Gunilla Andersson,<sup>||</sup> Anders Åberg,<sup>||</sup> Alan V. Wallace,<sup>⊥</sup> Garrett M. Morris,<sup>‡</sup> Arthur J. Olson,<sup>‡</sup> Dennis J. Stuehr,<sup>§</sup> John A. Tainer,<sup>‡</sup> and Elizabeth D. Getzoff<sup>\*‡</sup>

Department of Molecular Biology and Skaggs Institute for Chemical Biology, The Scripps Research Institute, 10550 North Torrey Pines Road, MB-4, La Jolla, California 92037, Department of Immunology, Lerner Research Institute, The Cleveland Clinic, 9500 Euclid Avenue, Cleveland, Ohio 44195, AstraZeneca Structural Chemistry Laboratories, Pepparedsleden 1, 431 83 Mölndal, Sweden, and AstraZeneca R&D Charnwood, Bakewell Road, Loughborough, Leicestershire LE11 5RH, U.K.

Received June 18, 2002; Revised Manuscript Received September 18, 2002

**ABSTRACT:** Nitric oxide is a key signaling molecule in many biological processes, making regulation of nitric oxide levels highly desirable for human medicine and for advancing our understanding of basic physiology. Designing inhibitors to specifically target one of the three nitric oxide synthase (NOS) isozymes that form nitric oxide from the L-Arg substrate poses a significant challenge due to the overwhelmingly conserved active sites. We report here 10 new X-ray crystallographic structures of inducible and endothelial NOS oxygenase domains cocrystallized with chlorzoxazone and four nitroindazoles: 5-nitroindazole, 6-nitroindazole, 7-nitroindazole, and 3-bromo-7-nitroindazole. Each of these bicyclic aromatic inhibitors has only one hydrogen bond donor and therefore cannot form the bidentate hydrogen bonds that the L-Arg substrate makes with Glu371. Instead, all of these inhibitors induce a conformational change in Glu371, creating an active site with altered molecular recognition properties. The cost of this conformational change is ~1–2 kcal, based on our measured constants for inhibitor binding to the wild-type and E371A mutant proteins. These inhibitors derive affinity by  $\pi$ -stacking above the heme and replacing both intramolecular (Glu371–Met368) and intermolecular (substrate–Trp366) hydrogen bonds to the  $\beta$ -sheet architecture underlying the active site. When bound to NOS, high-affinity inhibitors in this class are planar, whereas weaker inhibitors are nonplanar. Isozyme differences were observed in the pterin cofactor site, the heme propionate, and inhibitor positions. Computational docking predictions match the crystallographic results, including the Glu371 conformational change and inhibitor-binding orientations, and support a combined crystallographic and computational approach to isozyme-specific NOS inhibitor analysis and design.

A major challenge of modern medicine is to design compounds that modulate specific enzymes while leaving related isozymes unaffected. Three homologous NOS<sup>1</sup> isozymes [inducible NOS (iNOS), endothelial NOS (eNOS), and neuronal NOS (nNOS)] catalyze the five-electron, two-step oxidation of L-arginine (L-Arg) to form nitric oxide, an important biological signaling molecule and cellular cytotoxin (1–3). The constitutive isozymes, eNOS and nNOS, function to produce low levels of nitric oxide predominantly

for blood pressure regulation and nerve function, respectively. In contrast, iNOS is induced in response to cytokines and some pathogens to generate large, cytotoxic bursts of nitric oxide that can mediate inflammation and an innate immune response (4–7). iNOS inhibitors are potentially useful for treating sepsis, neurodegenerative disorders, diabetes, and arthritis. To have therapeutic value, however, NOS inhibitors must be isozyme selective, so interference with other nitric oxide signaling pathways is avoided (2). In particular, iNOS and nNOS inhibitors must not interfere with blood pressure regulation and vasodilation mediated by eNOS.

NOSs are homodimeric enzymes consisting of two conserved modules: an electron-supplying reductase module, homologous to cytochrome P450 reductase, with binding sites for NADPH, FAD, and FMN, and a catalytic oxygenase module (NOS<sub>ox</sub>), which binds the two cofactors, heme and 5,6,7,8-(6R)-tetrahydrobiopterin (BH4), a structural zinc metal, and the substrate L-Arg (8). The overall folds and active site structures are virtually identical in all three NOS<sub>ox</sub> isozymes (9–11; A. S. Arvai, J. A. Tainer, and E. D. Getzoff, unpublished results), and thus, NOS isozyme-specific inhibition presents a significant challenge for structure-based drug design.

<sup>†</sup> This work was supported by National Institutes of Health Grants HL58883 (E. D. Getzoff and D.J.S.) and RR08605 (A.J.O.) and fellowships from the Skaggs Institute for Chemical Biology (R.J.R. and E. D. Garcin), the La Jolla Interfaces in Science (R.J.R.), and the American Heart Association (E. D. Garcin).

\* To whom correspondence should be addressed. E-mail: edg@scripps.edu. Phone: (858) 784-2878. Fax: (858) 784-2289.

<sup>‡</sup> The Scripps Research Institute.

<sup>§</sup> The Cleveland Clinic.

<sup>||</sup> AstraZeneca Structural Chemistry Laboratories.

<sup>⊥</sup> AstraZeneca R&D Charnwood.

<sup>1</sup> Abbreviations: NOS, nitric oxide synthase; iNOS, inducible NOS; eNOS, endothelial NOS; nNOS, neuronal NOS; NOS<sub>ox</sub>, NOS oxygenase; iNOS<sub>ox</sub>, inducible NOS oxygenase; eNOS<sub>ox</sub>, endothelial NOS oxygenase; CHLZ, chlorzoxazone; 5NI, 5-nitroindazole; 6NI, 6-nitroindazole; 7NI, 7-nitroindazole; 3Br7NI, 3-bromo-7-nitroindazole; L-Arg, L-arginine; BH4, 5,6,7,8-(6R)-tetrahydrobiopterin.

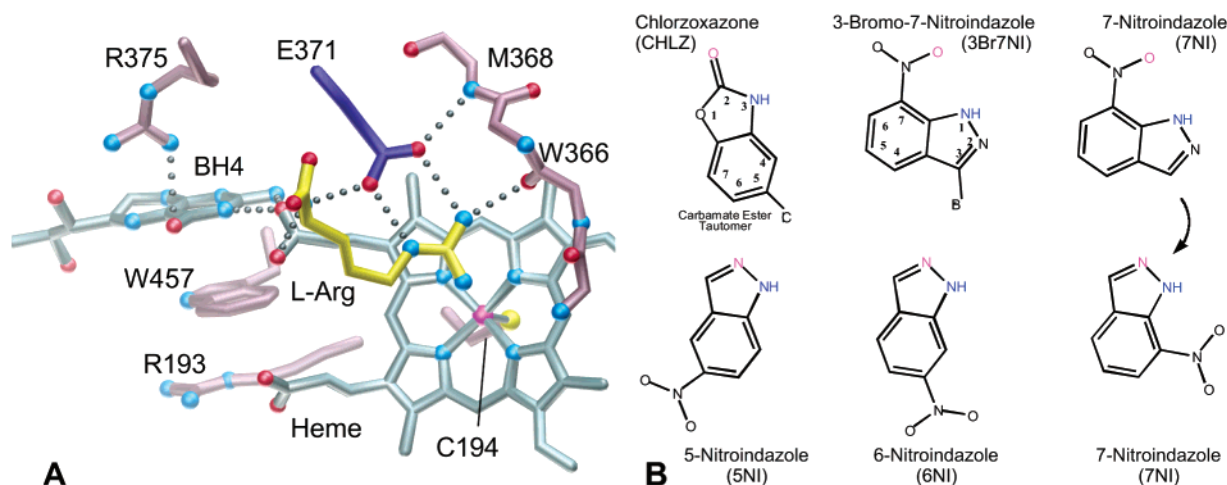


FIGURE 1: iNOS<sub>ox</sub> active site and inhibitors. (A) Structure of the substrate-bound iNOS<sub>ox</sub> active site showing hydrogen bonds that link the substrate, Glu371, heme, and BH4. Hydrogen bonds to the main chain Met368 amide nitrogen and Trp366 carbonyl oxygen anchor the active site Glu371 and substrate L-Arg to the underlying  $\beta$ -sheet. (B) Chlorzoxazone and the nitroindazole inhibitors, unable to form bidentate hydrogen bonds with Glu371, induce a conformational change in Glu371. The inhibitors are oriented approximately as they bind in the NOS active site, as depicted in panel A. Hydrogen-bonding partners for the Met368 amide and the Trp366 carbonyl are highlighted in magenta and blue, respectively.

The NOS<sub>ox</sub> dimer has a distinctive and unusual winged  $\beta$ -sheet architecture, with each monomer having a fold similar to a left-handed catcher's mitt (10, 12). The substrate-binding pocket, located on the distal side of the heme, is a 30 Å deep funnel that extends from an ellipsoidal inlet  $\sim 9$  Å  $\times$  15 Å back to zigzagged  $\beta$ -strands (10). The back wall of the active site is held within the rigid winged  $\beta$ -sheet architecture. Glu371 (murine iNOS<sub>ox</sub> numbering) is the only charged residue in the otherwise primarily hydrophobic interior of the substrate binding pocket and was shown by mutagenesis (E371A mutant) (13, 14) and structural analysis (10, 11) to be critical for the binding of substrate and substrate-analogue inhibitors. In the substrate-bound structure, four hydrogen bonds hold the Glu371 side chain carboxylate in place: two to the substrate L-Arg guanidinium group, one to the L-Arg main chain nitrogen, and one to the Met368 peptide nitrogen (Figure 1A). The compact hydrogen bonding network, shown in Figure 1A, which is formed among Glu371, L-Arg, Met368, and Trp366, mutually stabilizes both the position of the Glu371 side chain and the substrate L-Arg guanidinium and, furthermore, defines the binding mode of many NOS inhibitors such as those containing isothiourea or guanidinium moieties (9–11, 15–18).

Nitroindazoles are a unique class of NOS inhibitors because they lack functional groups capable of forming typical substrate-like hydrogen bonds with NOS<sub>ox</sub> (Figure 1B). These inhibitors exhibit low isozyme selectivity in vitro. However, some nitroindazoles exhibit in vivo isozyme selectivity, which has been attributed to their pharmacological properties (19). For instance, 7NI has been shown to alleviate cerebral ischemic injury by selectively inhibiting nNOS in murine and rat models (20). CHLZ (5-chloro-2-hydroxybenzoxazole), which has a planar ring system reminiscent of nitroindazoles, also has been reported to inhibit NOS (21). CHLZ has a long history of use as a skeletal muscle relaxant in humans (22, 23). Neither CHLZ nor nitroindazoles have functional groups that can form bidentate hydrogen bonds with Glu371, a characteristic of substrate-mimetic NOS inhibitor binding. In fact, each of these compounds has only

one hydrogen bond donating group available (Figure 1B). Therefore, these inhibitors were chosen for structural analysis because we anticipated that they would bind in a manner different from that of substrate-mimetic inhibitors.

Recent studies reported that 7NI and 3Br7NI induce a conformational change in NOS<sub>ox</sub> Glu371 (murine iNOS numbering) (24–26). However, important questions remain. What is the structural basis for affinity differences for inhibitors that induce a conformational change in Glu371? Is this mechanism of NOS inhibition conserved across isoforms? Are there isozyme-specific differences in inhibitor binding or conformational changes? What are the energetic costs for the Glu371 conformational change? To address these questions, we determined 10 X-ray structures of iNOS<sub>ox</sub> and eNOS<sub>ox</sub> cocrystallized with a series of four nitroindazoles and a chemically related drug, CHLZ (Figure 1B). These compounds have a wide range of inhibitor potencies (from  $\sim 200$  nM to  $> 1$  mM) and were thus useful for probing the structural basis of NOS inhibitor affinity within this class. To estimate the energetic costs of the conformational change in Glu371, we measured the inhibitor-binding affinities to wild-type iNOS<sub>ox</sub> and to the substrate binding site mutant, E371A (14), which should not require a conformational change. Finally, to computationally characterize how inhibitor binding interactions compensate for the energetic costs of the Glu371 conformational change, we created a computational model of the iNOS<sub>ox</sub> active site with a flexible Glu371 side chain and examined the automated docking of inhibitors.

## EXPERIMENTAL PROCEDURES

**Crystallography.** Human eNOS<sub>ox</sub>  $\Delta 76$  (residues 77–482) was expressed and purified in a manner similar to a previously described protocol (9), with the exceptions being that the construct did not contain a GST fusion tag and was purified in a single step using a heparin column. Murine iNOS<sub>ox</sub>  $\Delta 65$  (residues 66–498) was expressed in *Escherichia coli* and purified as previously described (27). Inhibitor (2–5 mM) was added to a 15 mg/mL solution of iNOS<sub>ox</sub> protein

in 40 mM *N*-(2-hydroxyethyl)piperazine-*N'*-(3-propanesulfonic acid) (EPPS) (pH 7.6), 1 mM dithiothreitol, and 2  $\mu$ M BH4. Cocrystals of iNOS<sub>ox</sub> were grown in the *P*6<sub>1</sub>22 space group ( $a = b = 214$  Å,  $c = 115$  Å) at 4 °C by vapor diffusion against a reservoir containing 20–30% Li<sub>2</sub>SO<sub>4</sub>, 5% *n*-octyl  $\beta$ -glucopyranoside ( $\beta$ OG), and 50 mM 2-(*N*-morpholino)ethanesulfonic acid (MES) (pH 5.3) (10). Inhibitor (2–5 mM) was added to a solution containing 20 mg/mL eNOS<sub>ox</sub> in 25 mM Tris (pH 8.0), 400 mM NaCl, 4 mM dithiothreitol, and 10  $\mu$ M BH4. eNOS<sub>ox</sub> inhibitor cocrystals in the *P*2<sub>1</sub>2<sub>1</sub> space group were grown by vapor diffusion at room temperature against reservoirs containing sodium acetate at pH 5.0–6.0 in 200–400 mM NaCl, 13% 2-methyl-2,4-pentanediol (MPD) or 2-propanol, and 2–5% polyethylene glycol 3350 (9). Crystals were mounted in loops, soaked for approximately 15 s in cryoprotectant solutions containing 30% glycerol and 15% MPD for iNOS<sub>ox</sub> and eNOS<sub>ox</sub>, respectively, and then frozen directly in a cryostream. X-ray diffraction data were collected at SSRL BL 9-1, SSRL BL 7-1, and APS BL 5.0.2 at 100 K using synchrotron radiation. Data were processed using Denzo and Scalepack (28). The previously reported dimeric iNOS<sub>ox</sub> structure (PDB entry 1DF1) with isothioureia, waters, and cofactors removed was used as an initial refinement model (15). Inhibitors were fit into  $F_o - F_c$  electron density, and the overall structures were refined through multiple iterative cycles in CNS (29) and manual fitting with xfit (30).

**Mutagenesis and Binding Assays.** The E371A mutant of iNOS<sub>ox</sub> was expressed and purified as previously described (31, 32). Inhibitor binding to wild-type and E371A iNOS<sub>ox</sub> was assessed spectroscopically in competition against cyanide (33). Optical spectra were recorded at room temperature on a Hitachi U-2110 spectrophotometer. Both the wild-type and mutant enzymes were incubated overnight with 10  $\mu$ M BH4 at 4 °C and then with 30 mM KCN for 15 min at room temperature. Each sample was titrated with inhibitor, and the absorbance change ( $\Delta A$ ) was recorded at 438 nm, 15 min after each addition. Apparent  $K_d$  values were determined from the double-reciprocal Lineweaver–Burke plot of  $1/\Delta A$  versus  $1/[\text{inhibitor}]$ .  $K_d$  values were calculated using the equation  $K_d = K_d^{\text{apparent}}/(1 + [\text{CN}]/K_d^{\text{CN}})$ , where  $K_d^{\text{CN}} = 10$  mM (34).

**Automated Docking.** Polar hydrogens and Kollman united atom charges (35, 36) were added to the NOS<sub>ox</sub> dimer models using QUANTA (Molecular Simulations, San Diego, CA). Solvation parameters were added in the final column of the protein coordinate files in accordance with the AutoDock force field (37). Standard AutoDock atomic radii and well-depth potentials were used for protein and ligand atoms (37). Affinity grid maps with 0.375 Å spacing and 40 points in each direction were computed for each ligand atom type and electrostatics by using AutoGrid 3.0. These maps were centered on a point above the heme iron in the active site and calculated using the rigid portion of the protein (i.e., without the Glu371 side chain). Glu371 was modeled as a flexible residue, and for this reason, its side chain was left out of the grid map calculations. Instead, the Glu371 side chain was included in the ligand PDBQ file, using “BEGIN-RES” and “END-RES” tokens to distinguish it from the moving, reorienting ligand. The new tokens “BEGIN-RES” and “END-RES” are used by AutoDock 4.0 (developmental version in preparation for release) to indicate flexible protein

side chains. In this way, the Glu371 side chain is docked in parallel with the ligand, with added constraints to maintain the bond between the flexible side chain and the polypeptide backbone. A file was created to specify the ligand, flexible side chain, and torsional degrees of freedom using the Python-based AutoDockTools graphical user interface (<http://www.scripps.edu/~olson>) (38).

The ligand and Glu371 side chain were simultaneously docked to the iNOS<sub>ox</sub> rigid protein grid maps for 100 trials using a Lamarckian genetic algorithm within AutoDock 4.0. Each trial docking was initiated with a population consisting of 50 randomly generated positions, orientations, and conformations of the ligand and 50 randomly generated conformations of the flexible side chain. We used the default AutoDock Lamarckian genetic algorithm parameters: 4% point mutation rate, 80% crossover rate, and 6% local search probability (37). Dockings were performed on SGI IRIX Release 6.3 IP21 with R10000 processor chips operating at 90 MHz. Resulting docked orientations within a 1.0 Å rmsd tolerance of each other were clustered together, and clusters containing more than 10 dockings out of 100 trials were considered the predominant predicted conformations. The final structures, the rmsd from the bound crystal structure, the docked energy, and the predicted free energy of binding were reported in the AutoDock output for each cluster and each individual docking. Docked conformations were analyzed using the Python-based AutoDock Tools graphical user interface (38).

A model for E371A was created by truncating the Glu371 side chain. E371A grid maps were computed and inhibitors docked to E371A as described above, with the exception that, in the absence of the Glu371 side chain, the entire protein was modeled as a rigid body using AutoDock version 3.0 (37). Ten docking trials were deemed sufficient for this simpler system, and this was justified by the high degree of clustering that was observed.

## RESULTS

**CHLZ and Nitroindazoles Bound to eNOS<sub>ox</sub> and iNOS<sub>ox</sub> Active Sites.** To determine how inhibitors that lack guanidinium-like functional groups bind in a site designed for the L-Arg substrate, we determined crystallographic structures of eNOS<sub>ox</sub> and iNOS<sub>ox</sub> complexed with CHLZ and four nitroindazole inhibitors (Figure 1 and Tables 1 and 2). These five aromatic inhibitors are bicyclic, with one six-carbon ring bearing an electron-withdrawing substituent and one five-membered ring containing two heteroatoms (oxygen or nitrogen). Each of these inhibitors has only one hydrogen bond donating group. The crystal structures of the inhibitors bound to eNOS<sub>ox</sub> and iNOS<sub>ox</sub> are superimposed in Figure 2. In all 10 complexes, the inhibitor stacks above the heme in the L-Arg binding site and displaces Glu371, which otherwise provides the negatively charged bidentate ligand for the substrate guanidinium group. With the exception of 5NI, these inhibitors form hydrogen bonds with both the NOS Trp366 carbonyl and Met368 amide (murine iNOS numbering). Yet, these inhibitors differ in their orientation within the active site, their preference for a single binding orientation, their geometry and length of hydrogen bonds with the protein, and their efficiency of  $\pi$ -stacking with the heme.

These inhibitors are herein classified as “O–N” or “N–N” binders on the basis of their division into two hydrogen



Table 1: eNOS<sub>ox</sub> Data Collection and Refinement Statistics

structure (PDB accession code)	eNOS-7NI (1M9K)	eNOS-CHLZ (1M9J)	eNOS-6NI (1M9M)	eNOS-5NI (1M9Q)	eNOS-3Br7NI (1M9R)
scatterers	6838	6629	6915	6876	6679
residues	2 × (77–115, 130–490)	2 × (77–115, 130–490)	2 × (77–115, 130–490)	2 × (77–115, 130–490)	2 × (77–115, 130–490)
cofactors	2 hemes	2 hemes	2 hemes	2 hemes	2 hemes
ligands	2 7NI	2 CHLZ	2 6NI	2 5NI	4 3Br7NI
waters	335	146	413	395	172
resolution (Å)	20.0–2.01 (2.08–2.01) <sup>a</sup>	20.0–2.43 (2.52–2.43)	50.0–1.96 (2.01–1.96)	50.0–2.01 (2.06–2.01)	50.0–2.55 (2.64–2.55)
unique reflections	66080 (6469)	34536 (3376)	69487 (4142)	67869 (4490)	30462 (2989)
observations	247064 (21274)	181549 (18071)	290276 (8898)	308827 (15119)	127718 (12185)
completeness (%)	99.0 (98.6)	89.9 (89.4)	96.6 (87.2)	99.4 (99.8)	96.1 (95.6)
$\langle I/\sigma I \rangle^b$	31.9 (5.9)	21.1 (5.3)	28.4 (2.7)	30.5 (4.4)	22.8 (5.2)
$R_{\text{sym}} (\%)^c$	4.2 (23.9)	8.0 (42.5)	4.6 (32.1)	5.5 (31.5)	6.3 (19.3)
$R (\%)^d$	19.8	21.6	19.2	20.2	20.7
$R_{\text{free}} (\%)^e$	22.3	27.1	22.3	23.3	26.5
average $B$ (Å <sup>2</sup> )	33.3	39.8	38.6	37.7	48.1
rmsd for bonds (Å)	0.006	0.008	0.006	0.006	0.009
rmsd for angles (deg)	1.3	1.2	1.3	1.3	1.2

<sup>a</sup> Highest-resolution shell for compiling statistics. <sup>b</sup> Average-intensity signal-to-noise ratio. <sup>c</sup>  $R_{\text{sym}} = \sum_j |I_j - \langle I \rangle| / \sum_j I_j$ . <sup>d</sup>  $R = \sum ||F_o| - |F_c|| / \sum |F_o|$ , where  $F_o$  and  $F_c$  are the observed and calculated structure factors, respectively. <sup>e</sup> Five percent of the reflections were set aside randomly for the  $R_{\text{free}}$  calculation.

Table 2: iNOS<sub>ox</sub> Data Collection and Refinement Statistics

structure (PDB accession code)	iNOS-7NI (1M8E)	iNOS-CHLZ (1M8D)	iNOS-6NI (1M8H)	iNOS-5NI (1M8I)	iNOS-3Br7NI (1M9T)
scatterers	7066	7384	6956	6980	7143
residues	77–101, 110–495	77–497	77–101, 110–495	77–101, 110–495	77–101, 110–495
	77–100, 109–495	77–497	77–100, 109–495	77–100, 109–495	77–100, 109–495
cofactors	2 hemes, 2 BH4	2 hemes, 2 BH4	2 hemes, 2 BH4	2 hemes, 2 BH4	2 hemes, 2 BH4
ligands	2 7NI	2 CHLZ	2 6NI	2 5NI	2 3Br7NI
waters	208	363	89	78	255
resolution (Å)	20.0–2.9 (3.0–2.9) <sup>a</sup>	20.0–2.35 (2.43–2.35)	20.0–2.85 (2.95–2.85)	20.0–2.7 (2.8–2.7)	20.0–2.4 (2.5–2.4)
unique reflections	34362 (3407)	61961 (5149)	31915 (2069)	36964 (2312)	59481 (5605)
observations	91396 (9346)	306715 (13672)	150303 (5405)	85604 (4659)	273885 (21320)
completeness (%)	99.1 (99.9)	95.6 (80.8)	88.5 (58.3)	86.6 (55.0)	99.1 (95.2)
$\langle I/\sigma I \rangle^b$	17.0 (3.1)	24.8 (2.5)	11.7 (1.8)	15.6 (2.5)	20.6 (3.6)
$R_{\text{sym}} (\%)^c$	5.4 (31.8)	5.8 (36.6)	12.5 (50.4)	6.0 (32.6)	7.0 (33.0)
$R (\%)^d$	22.8	24.5	24.3	24.0	24.9
$R_{\text{free}} (\%)^e$	27.5	27.4	29.0	28.1	28.3
average $B$ (Å <sup>2</sup> )	56.1	54.1	61.4	59.3	55.2
rmsd for bonds (Å)	0.008	0.009	0.008	0.008	0.008
rmsd for angles (deg)	1.4	1.3	1.4	1.3	1.3

<sup>a</sup> Highest-resolution shell for compiling statistics. <sup>b</sup> Average-intensity signal-to-noise ratio. <sup>c</sup>  $R_{\text{sym}} = \sum_j |I_j - \langle I \rangle| / \sum_j I_j$ . <sup>d</sup>  $R = \sum ||F_o| - |F_c|| / \sum |F_o|$ , where  $F_o$  and  $F_c$  are the observed and calculated structure factors, respectively. <sup>e</sup> Five percent of the reflections were set aside randomly for the  $R_{\text{free}}$  calculation.

bonding configurations (Figure 2). In both the O–N and N–N binding modes, an inhibitor nitrogen atom serves as a donor of a hydrogen bond to the Trp366 carbonyl oxygen. The two binding modes differ in whether an inhibitor oxygen atom (O–N) or nitrogen atom (N–N) serves as the hydrogen bond acceptor for the Met368 amide nitrogen.

According to our crystal structures, CHLZ and 3Br7NI bind in O–N configurations (Figure 3). The nitro group oxygen of 3Br7NI hydrogen bonds to the Met368 amide, occupying the native position of the Glu371 side chain, while the protonated ring nitrogen (N1) hydrogen bonds to the Trp366 carbonyl (Figure 3A,C). CHLZ, oriented in a manner similar to that of 3Br7NI, forms a hydrogen bond between the exocyclic oxygen and the Met368 amide (Figure 3B,D). To make these hydrogen bonds, the protein converts CHLZ to the carbamate ester tautomer (Figure 1B).

6NI and 5NI bind in N–N configurations (Figure 2, right). Besides the protonated ring nitrogen hydrogen bond to the

Trp366 carbonyl, 6NI forms a hydrogen bond between its unprotonated ring nitrogen and the Met368 amide. 5NI is best classified as an N–N binder; however, 5NI does not fully meet the hydrogen bonding criteria. 5NI forms N–N hydrogen bonds with eNOS<sub>ox</sub>, but does not hydrogen bond at all to iNOS<sub>ox</sub>. An isozyme-specific difference in the position of Val346, a conserved active site residue against which the nitro group is packed, prevents 5NI from hydrogen bonding with iNOS<sub>ox</sub>. The Val346 side chain extends 0.8 Å further into the iNOS<sub>ox</sub> active site than into the eNOS<sub>ox</sub> active site, causing a subtle but significant isozyme-specific shift in the position of 5NI, which abolishes hydrogen bonds to iNOS<sub>ox</sub>.

7NI, evidently, has a dual N–N/O–N binding mode (Figure 4A). The two binding modes are related by pseudo-2-fold symmetry. In both orientations, the protonated ring nitrogen (N1) is positioned to hydrogen bond with the Trp366 carbonyl. The hydrogen bond with the Met368 amide is

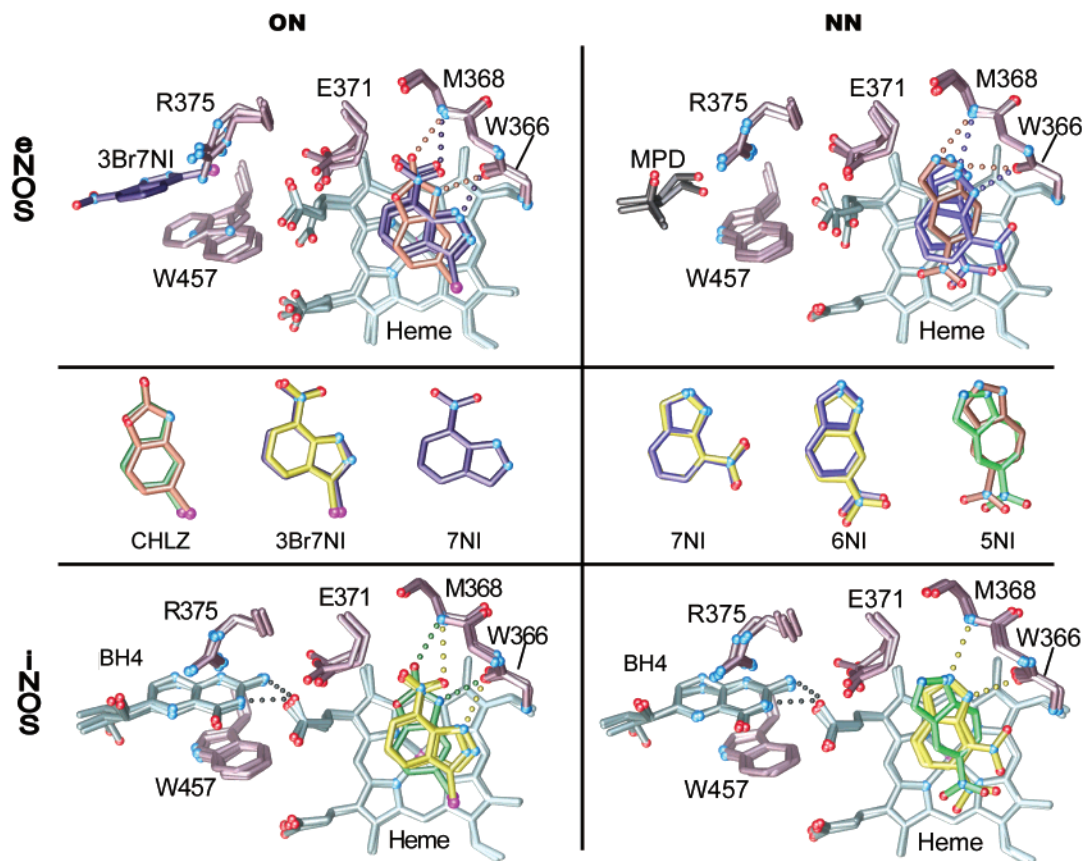


FIGURE 2: Structures of eNOS<sub>ox</sub> (top) and iNOS<sub>ox</sub> (bottom) cocrystallized with CHLZ and nitroindazoles, with eNOS<sub>ox</sub>/iNOS<sub>ox</sub> active site inhibitor orientations superimposed (middle). For each isozyme, the structures of NOS<sub>ox</sub> inhibitor complexes are superimposed in groups according to the inhibitor atoms hydrogen bonding with the Met368 amide nitrogen and the Trp366 carbonyl oxygen (O–N, left; N–N, right). Hydrogen bonds are shown for CHLZ, 7NI, and 5NI as small spheres colored the same as each inhibitor. All of these inhibitors induced a conformational change in Glu371. Note the following isozyme-specific differences: relative rotation of 5NI in eNOS<sub>ox</sub>/iNOS<sub>ox</sub> (far right, middle), BH4 not bound in any of the eNOS<sub>ox</sub> structures (top), and BH4 bound in all of the iNOS<sub>ox</sub> structures (bottom). Heme propionate A exhibits a greater range of conformational change in eNOS<sub>ox</sub>, relative to iNOS<sub>ox</sub>.

satisfied in the O–N conformation by an oxygen atom from the nitro group, and in the N–N conformation by the unprotonated ring nitrogen (N2). The shape of the density for 7NI (note the flattened, nearly triangular region at the lower right in Figure 4A) indicates a slight preference for the N–N configuration. Modeling the inhibitor occupancy as 60% N–N and 40% O–N, in fact, minimized the difference density, and suggests that the interaction energy for these two modes may be similar. It is interesting to note that 3Br7NI is sterically prevented from binding in an N–N orientation by the bromine atom, which would collide with Glu371 in the N–N binding mode.

Inhibitor differences in the extent of  $\pi$ -stacking with the heme relate to inhibitor chemistry and binding affinity. CHLZ, 3Br7NI, and 7NI are planar when bound and  $\pi$ -stack efficiently above the heme. CHLZ and 3Br7NI bind with their halide atoms above heme pyrrole ring C, offset from the pyrrole nitrogen. In this position, some electrostatic stabilization of the halides is provided by the amides of Gly365 and Val346. 6NI and 5NI, the weaker inhibitors in this class, bind with their nitro groups rotated 50° and 40°, respectively, out of the plane of the indazole ring (Figure 2). Therefore, more potent inhibitors (CHLZ, 3Br7NI, and 7NI)  $\pi$ -stack more efficiently with the heme than low-affinity inhibitors (6NI and 5NI), which exhibit decreased aromaticity, indicated by nonplanarity when bound. Finally, we

observed differences in the extent of inhibitor occupancy in the active site. CHLZ, 3Br7NI, and 7NI have full inhibitor occupancy. In contrast, the electron density for 5NI suggests incomplete inhibitor occupancy (85%), and the electron density for 6NI suggests alternate inhibitor conformations with low occupancy (<10%) that contribute to binding.

**Glu371-Induced Conformational Change.** Each of these five inhibitors induces a conformational change in the side chain of Glu371 (Figure 2), regardless of the position of the inhibitor nitro group. In both iNOS<sub>ox</sub> and eNOS<sub>ox</sub>, the Glu371 side chain rotates toward heme propionate A and forms new hydrogen bonds with structural waters.

Despite the same inhibitor-induced Glu371 conformational change in iNOS<sub>ox</sub> and eNOS<sub>ox</sub>, further conformational changes are propagated isozyme-specifically to the heme propionate. In iNOS<sub>ox</sub>, the position of heme propionate A remains nearly constant, held in place by hydrogen bonds to BH4 N2 and N3. The pairwise rmsds for atoms in iNOS<sub>ox</sub> propionate A in the five structures range from 0.13 to 0.37 Å (average rmsd of 0.19 Å). However, in eNOS<sub>ox</sub>, the position of heme propionate A varies to a greater extent (pairwise rmsds range from 0.36 to 1.64 Å, average rmsd of 0.89 Å) (Figure 2). For example, in the CHLZ-bound eNOS<sub>ox</sub> structure, the heme carboxylate group is rotated 20°, and hydrogen bonds with two structural waters, one of which introduces a water-mediated hydrogen bond to Arg375. A

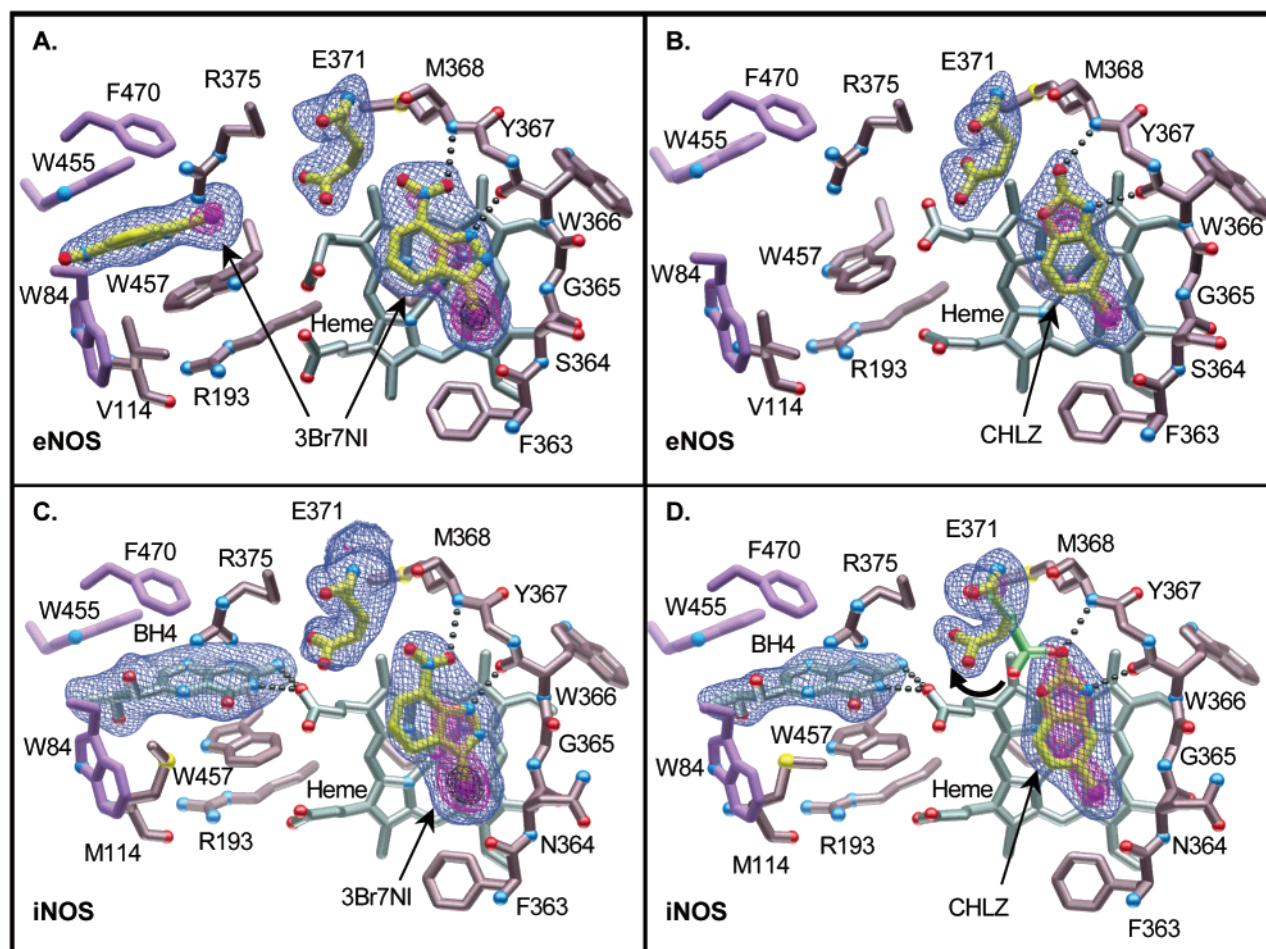


FIGURE 3: eNOS<sub>ox</sub> and iNOS<sub>ox</sub> active site electron density showing the conformational change of Glu371 upon inhibitor binding.  $F_o - F_c$  electron density maps with the inhibitor, Glu371, and BH4 omitted are shown contoured at  $4\sigma$ ,  $10\sigma$ , and  $18\sigma$  (blue, magenta, and black, respectively). (A) 3Br7NI binding to eNOS<sub>ox</sub> in the active site and the BH4 binding site, with additional conformational changes in heme propionate A and Trp457. (B) CHLZ binding to the eNOS<sub>ox</sub> active site. (C) 3Br7NI binding to the iNOS<sub>ox</sub> active site. (D) CHLZ binding to the iNOS<sub>ox</sub> active site. The native position of Glu371 is illustrated in green, and the inhibitor-induced conformational change is highlighted with an arrow.

more drastic change is seen in the 3Br7NI-bound eNOS<sub>ox</sub> structure, where the heme propionate points directly at the other heme propionate group (Figure 3A).

**Pterin Site Occupancy by BH4, Inhibitor, or Solvent.** In the five iNOS<sub>ox</sub>–inhibitor structures, BH4 remains bound with its conformation unperturbed from its orientation in the substrate-bound structure (Figure 2, bottom). However, in all five eNOS<sub>ox</sub> structures, BH4 is displaced and the pterin site is occupied by either an inhibitor, cryoprotectant, or structural waters (Figure 2, top). For example, 3Br7NI binds to the eNOS<sub>ox</sub> pterin-binding site, in addition to the active site (Figure 3A). In the pterin-binding site of eNOS<sub>ox</sub>, the position of the bromine of 3Br7NI is well-defined ( $6\sigma$ ). 3Br7NI does not form any hydrogen bonds within the pterin-binding site of eNOS<sub>ox</sub>. The binding affinity for 3Br7NI is thus derived from  $\pi$ -stacking and an electrostatic interaction between the bromine atom and Arg375 side chain. Structures of eNOS<sub>ox</sub> in complex with 5NI and 6NI have MPD bound in the pterin site, near the Trp455 side chain and Phe470 carbonyl.

**Automated Docking.** To better understand the biophysical forces acting in nitroindazole binding, we used an automated docking program to computationally dock each inhibitor into the iNOS<sub>ox</sub> active site (AutoDock 4.0). An advantage of

AutoDock 4.0 was that we were able to create a model of the iNOS<sub>ox</sub> active site with a flexible Glu371 side chain. To accomplish this, prior to docking, the rigid portion of the protein was used to calculate the affinity for each inhibitor atom type at grid points within the active site (Figure 4B). Glu371 was not used in the grid map calculation, but instead docked in unison with the inhibitor using a Lamarckian genetic algorithm. Our calculated affinity maps show that aromatic stacking with the heme and hydrogen bonding with Met368 and Trp366 dominate inhibitor docking in our calculated model of the NOS<sub>ox</sub> active site (Figure 4B).

Our docking results closely match our crystallographic results, suggesting that this computational method captures key features of molecular recognition (Table 3). Consistent with our crystallographic analyses, 3Br7NI and CHLZ docked almost exclusively to an O–N orientation, while 7NI docked to both N–N and O–N orientations (Figure 4B). In fact, the difference between the predicted interaction energies of 7NI in the N–N and O–N orientations (0.3 kcal/mol) was negligible within the AutoDock force field (2.8 kcal/mol standard error in the force field). 6NI and 5NI docked into a greater number of unique clusters relative to the other nitroindazole inhibitors. This is consistent with the X-ray crystallographic analyses in which we found evidence of



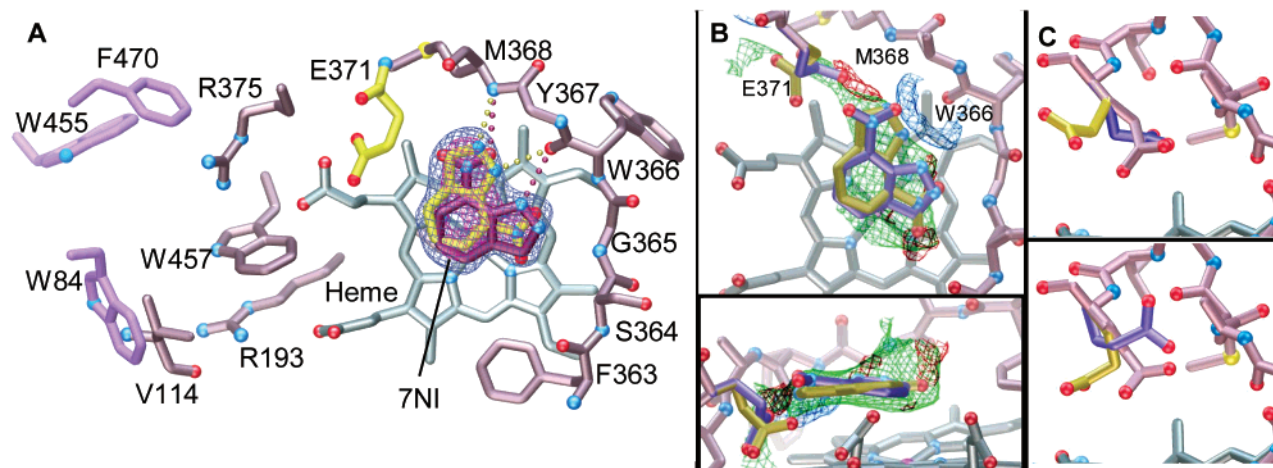


FIGURE 4: 7NI binds to NOS<sub>ox</sub> in a dual O-N/N-N binding mode. (A) The crystal structure of 7NI bound to eNOS<sub>ox</sub> with omit  $F_o - F_c$  electron density (blue,  $5\sigma$ ; magenta,  $9\sigma$ ). The shape of the electron density around the nitro groups corresponds to the slight preference for the N-N binding mode (yellow) over the O-N binding mode (magenta). (B) Computationally predicted docked orientations of 7NI in the iNOS<sub>ox</sub> active site shown in the heme plane (top) and perpendicular to the heme plane (bottom). Computed affinity grid maps used during docking are shown for aromatic carbon (green,  $-0.55$  kcal), oxygen (red,  $-0.5$  kcal), and hydrogen (blue,  $-0.2$  kcal) atom types. (C) Superposition of Glu371 conformations showing that the three clusters of docked predictions (top) are similar to the three positions observed crystallographically (bottom); Glu371 positions are color-coded as follows: rose for substrate-bound (10), yellow for nitroindazole-induced, and blue for the  $\Delta 114$  monomer (12).

Table 3: AutoDock-Predicted Binding Orientations

inhibitor	O-N <sup>a</sup>	N-N <sup>a</sup>	other <sup>b</sup>	inhibitor	O-N <sup>a</sup>	N-N <sup>a</sup>	other <sup>b</sup>
CHLZ	93 (1) <sup>c</sup>	0	7 (1)	6NI	0	87 (7)	13 (7)
3Br7NI	90 (4)	3 (1)	7 (4)	5NI	0	16 (3)	84 (15)
7NI	54 (2)	31 (2)	15 (6)				

<sup>a</sup> The total number of times each conformation (O-N or N-N) was predicted (out of 100 trials) for each ligand. Predicted orientations for the inhibitors were grouped into O-N and N-N, based on the hydrogen bonding criteria outlined in the crystallographic analysis. <sup>b</sup> Orientations that did not hydrogen bond to the Trp366 carbonyl and the Met368 amide were classified as other. <sup>c</sup> Predicted binding orientations were clustered within a 1.0 Å rmsd tolerance. The number of clusters can be used to gauge the similarity of the resulting predictions within each orientation. Smaller numbers of clusters indicate better convergence. Conversely, having a greater number of clusters (e.g., 6NI in N-N) indicates a more heterogeneous distribution of predictions.

incomplete inhibitor occupancy and multiple conformations in the 5NI- and 6NI-NOS<sub>ox</sub> complexes.

We analyzed the predicted conformations of Glu371, which was modeled as a flexible side chain. The Glu371 conformational change observed crystallographically in the nitroindazole-bound structures was predicted in most cases. However, two alternative side chain positions were predicted: Glu371 rotated toward the Met368 amide and Glu371 close to its native position in L-Arg-bound NOS<sub>ox</sub> (Figure 4C). In both cases, a hydrogen bond between Glu371 and the Met368 amide is maintained. In the latter case, the distances between the Glu371 side chain and atoms in the NOS backbone are slightly shorter than the optimal internuclear separation distance used in the AutoDock force field. This suggests that the computed electrostatic and hydrogen bonding forces near Met368 are large enough to offset some calculated van der Waals penalties. These results underscore the high affinity of the Met368 amide for atoms with partial negative charge and/or hydrogen bond acceptors.

**E371A Mutant and Inhibitor Binding Affinity.** To estimate the energetic penalties for the experimentally observed and computationally predicted inhibitor-induced conformational change in Glu371, we measured and compared the binding

Table 4: Binding Constants ( $\mu$ M) for 7NI and CHLZ

inhibitor	wild-type iNOS <sub>ox</sub>	E371A
7NI <sup>a</sup>	250	25
CHLZ <sup>a</sup>	4.3	0.6
CHLZ <sup>b</sup>	3.7	0.5

<sup>a</sup> Calculated using the equation  $K_d = K_d^{\text{apparent}} / (1 + [\text{CN}]/K_i^{\text{CN}})$ , where  $K_d^{\text{apparent}}$  is measured in competition with 30 mM KCN. <sup>b</sup> Measured directly using  $\Delta A$  at 438 nm.

affinities of 7NI and CHLZ for E371A and wild-type iNOS<sub>ox</sub> (Table 4). The inhibitors bind approximately 10-fold better to E371A than to the wild type, which corresponds to an energy difference of approximately 1–2 kcal/mol. This indicates that (i) an energetic penalty is associated with rearranging Glu371 and/or (ii) the inhibitor binding orientation is less constrained in E371A than in the wild type. To test the latter, we docked CHLZ and 7NI to a model of E371A, which we constructed from the wild-type iNOS<sub>ox</sub> crystal structure. CHLZ and 7NI both docked in conformations matching those observed in the wild-type iNOS<sub>ox</sub> cocrystallized inhibitor complexes. Specifically, the O-N orientation was predicted for CHLZ, and both the N-N and O-N orientations were predicted for 7NI, with similar binding energies. Thus, the difference in binding free energy, estimated from the measured binding affinities to be 1–2 kcal/mol, largely reflects the energetic cost of the inhibitor-induced conformational change in Glu371.

## DISCUSSION

*$\pi$ -Stacking Is a Determining Factor in Nitroindazole Inhibitor Potency.* Inhibitor potency for the nitroindazoles and CHLZ correlates with the relative efficiency of  $\pi$ -stacking observed in our NOS<sub>ox</sub> inhibitor structures (Figure 2). The common structural feature we observe for all of the high-affinity inhibitors (CHLZ, 3Br7NI, and 7NI) is planar binding to the heme in both iNOS<sub>ox</sub> and eNOS<sub>ox</sub>. The common structural feature of the weaker inhibitors, 6NI and 5NI, is nonplanarity when bound. Rotation of the nitro groups of

5NI and 6NI out of the indazole plane was unexpected because it disrupts what we anticipated to be a stable aromatic system, and presumably would be associated with a significant energetic penalty. However, such rotations between nitro groups and aromatic rings are commonly seen in small molecule crystal structures (39, 40). Steric constraints of the NOS<sub>ox</sub> active site, imposed by the side chains of Val346 and Phe363, likely promote rotation of the 5NI and 6NI nitro groups out of the indazole ring plane and thereby decrease the efficiency of  $\pi$ -stacking with the heme.

The structural results reported here support previous proposals that the nitro group enhances NOS inhibition by serving as an electron-withdrawing substituent (41), rather than recent suggestions that the nitro group is required primarily as a hydrogen bonding group (24). First, hydrogen bonding interactions with the nitro group are not absolutely essential for this type of molecular recognition by NOS, since we observed no hydrogen bonds between NOS<sub>ox</sub> and the nitro groups of 5NI, 6NI, or 7NI in the N–N configuration. Second, the inhibitor–heme  $\pi$ -stacking interaction that we observe in our structures would be strengthened by an electron-withdrawing group, according to theoretical models (42). Therefore, the primary function of the electron-withdrawing nitro group is to promote a favorable  $\pi$ -stacking interaction.

Our structures show that the nitroindazoles and CHLZ stack with the NOS<sub>ox</sub> heme in an offset configuration (Figure 2), which is the optimal geometry for  $\pi$ -stacking interactions according to theoretical models developed by Hunter and Sanders (42). The face-to-face configuration, where each atom binds directly over another atom, maximizes van der Waals overlap, but also maximizes electronic  $\pi$ – $\pi$  repulsion. The offset geometry minimizes electronic  $\pi$ – $\pi$  repulsion, while maintaining favorable van der Waals interactions (42). Aromatic stacking interactions are important noncovalent intermolecular forces that can contribute at least as much energy as hydrogen bonding (42–44). For example, the computed interaction energy for benzene stacking in an offset configuration is 4 kcal/mol (44), which is on the order of that of the typical hydrogen bonding interaction (3–6 kcal/mol). The magnitude of the stacking interaction energy is predicted to increase with increasing molecular size and extent of polarization (42–44). In our structures, stacking interactions are evidently strengthened by polarization created by the heme iron, and the nitro groups, ring nitrogens, and halide ions of the inhibitors. Therefore,  $\pi$ -stacking with the heme makes significant contributions to the inhibitor binding affinity.

*Hydrogen Bonds to the Trp366 and Met368 Backbone Orient Inhibitors in the Active Site.* The inhibitors described here mimic both intra- and intermolecular interactions observed in NOS<sub>ox</sub> substrate-mimetic bound structures by forming hydrogen bonds with both the Met368 amide nitrogen and the Trp366 carbonyl oxygen, which are part of the  $\beta$ -sheet architecture that underlies the active site. We observed two binding modes, N–N and O–N, named to define the hydrogen-bonding atoms in the inhibitor. Both the O–N and N–N binding modes can result in high-affinity inhibitor interactions. In fact, the dual O–N/N–N binding mode for 7NI was observed in our crystal structures and predicted in automated docking simulations. Our results differ significantly from recent reports in which a single O–N

binding orientation was assigned for 7NI (24), evidently based on 3Br7NI binding in the O–N configuration. However, one should not assume that 7NI would bind in the same way as 3Br7NI since the bulky bromine atom specifically precludes the N–N configuration for 3Br7NI. The experimentally and computationally defined dual binding mode that we found for 7NI suggests that the O–N/N–N configurations are nearly isoenergetic for this inhibitor. Thus, for this family of inhibitors that induce a Glu371 conformational change, as long as hydrogen bonds with Met368 and Trp366 are simultaneously satisfied, the identity of the hydrogen-bonding partners does not drastically alter inhibitor potency. The importance of the hydrogen bonds with Met368 and Trp366 in orienting inhibitors was also supported by the magnitude of the favorable interaction energies computed in the atomic affinity grid maps used for docking. Two of the three positions predicted for Glu371 in the course of our docking simulations oriented the side chain to satisfy a hydrogen bond with the Met368 amide nitrogen.

The hydrogen bonding pattern with Met368 and Trp366 establishes a structural framework for understanding the high (but non-isozyme-specific) binding affinity of CHLZ and the less potent inhibition by closely related analogues: zoxolamine and 6-hydroxy-CHLZ (21). There are no isozyme-specific contacts between CHLZ and NOS<sub>ox</sub> in our structures. This is reflected in the lack of isozyme-specific inhibition [CHLZ IC<sub>50</sub> values of 7, 9, and 13  $\mu$ M for human iNOS, eNOS, and nNOS, respectively, measured in the presence of 1  $\mu$ M L-Arg (21)]. CHLZ binds with high affinity because it meets the molecular recognition criteria by forming hydrogen bonds with the Met368 amide and Trp366 carbonyl, as well as a high-affinity  $\pi$ -stacking interaction with the heme. On the basis of the hydrogen bonding pattern, CHLZ evidently bound to NOS<sub>ox</sub> as the carbamate ester tautomer, reversing the expected hydrogen bonding roles of the 2-exocyclic oxygen as donor and the ring nitrogen as an acceptor (Figure 1B). Zoxolamine, which differs from CHLZ by substitution of an amino group for the 2-oxo, does not appreciably inhibit NO synthesis (21), presumably because the 2-amino group cannot serve as a hydrogen-bonding partner for the Met368 amide nitrogen. CHLZ is metabolized by cytochrome P450 in vivo to 6-hydroxy-CHLZ, which is 5-fold less potent than CHLZ (45). Two factors may contribute to the decreased potency of the 6-hydroxy analogue: a shift in the tautomer equilibrium and close contact between the 6-hydroxyl and Val346, either of which may disturb the Met368 and/or Trp366 hydrogen bonds. As we observed with 5NI, inhibitor packing against Val346 can cause shifts that disrupt hydrogen bonding. Therefore, 6-hydroxy-CHLZ and zoxolamine are less potent because they fail to satisfy hydrogen bonds with Met368 and/or Trp366 and/or meet the geometric constraints within the NOS<sub>ox</sub> active site.

*Low Energetic Barrier for Glu371 Conformational Change.* The 10 inhibitor-bound NOS<sub>ox</sub> complexes reported here clearly establish a recurring pattern of molecular recognition involving an induced conformational change in the Glu371 side chain (Figure 2). The 10-fold improved affinity for binding of inhibitors to the E371A iNOS<sub>ox</sub> mutant relative to that of the wild type indicates that the energetic cost of the inhibitor-induced conformational change in the Glu371 side chain is only  $\sim$ 1–2 kcal/mol, which can be offset by



hydrogen bonding and  $\pi$ -stacking. Although most NOS inhibitors are recognized via bidentate hydrogen bonds with Glu371, the hydrogen bonds between Glu371 and L-Arg have been estimated to be worth only  $<2$  kcal, less than the 3–6 kcal typically expected for hydrogen bonds (16). Although the Glu371 conformational change disrupts a hydrogen bond between Glu371 and Met368, high-affinity inhibitors that induce this conformational change also satisfy the hydrogen bond with Met368.

In agreement with crystallographic analyses, automated docking predictions also indicate a propensity for Glu371 to undergo conformational changes. The Glu371 side chain docked primarily to three positions: native, rotated toward heme propionate A, and rotated toward Met368. Interestingly, these three computationally defined Glu371 conformations correspond with the three Glu371 conformations observed in NOS<sub>ox</sub> crystal structures (Figure 4): the L-Arg-bound dimer (10), the nitroindazole-bound dimer, and the imidazole-bound  $\Delta$ 114 monomer (12), respectively. The last coincides with a peptide flip in Gly369 that has only been observed in the monomeric structure (12). Consistent with our analyses of dimeric NOS<sub>ox</sub> structures, ligand-induced conformational changes often involve discrete side chains and more rarely extend to rearrangements in backbone structure (46). The NOS<sub>ox</sub> active site, in particular, is part of a highly ordered winged  $\beta$ -structure that extends the length of the enzyme. Furthermore, of the side chains that extend into the NOS<sub>ox</sub> active site (Glu371, Val346, and Phe363), the glutamate has the highest propensity to undergo inhibitor-induced conformational change, based on the reported statistical analysis of side chain rotamers in ligand-bound and apo protein structures (46).

*Isozyme Specificity in the Pterin Sites of eNOS<sub>ox</sub> and iNOS<sub>ox</sub>.* Like others, we found evidence of non-pterin compounds in the eNOS<sub>ox</sub> BH4 binding site (9, 11, 24). In contrast, the BH4 binding sites of all currently published dimeric iNOS<sub>ox</sub> crystal structures, as well as the five new iNOS<sub>ox</sub>–inhibitor complexes reported here, have BH4 or a BH4 analogue bound with full occupancy (10, 15, 47–49). BH4 is even bound in crystal structures of iNOS<sub>ox</sub> pterin-binding site mutants, W457A and W457F (48). In our experience, BH4 is required for dimeric iNOS<sub>ox</sub> crystallization (unpublished results), while eNOS<sub>ox</sub> crystals grown in the presence of excess pterin appear to diffract to lower resolution than crystals grown under the same conditions without additional BH4 (24) (data not shown).

Isozyme-specific BH4 binding kinetics may result in selective crystallization of pterin-bound iNOS<sub>ox</sub> dimers, whereas eNOS<sub>ox</sub> dimers can crystallize without the pterin site occupied by BH4. Although the binding constants of BH4 to eNOS (147 nM) and iNOS (84 nM) are similar, the cofactor exchanges much faster in eNOS (50, 51). Binding studies have shown that radiolabeled BH4 dissociates more than 300-fold faster from eNOS ( $k_{\text{off}} = 1.6 \text{ min}^{-1}$ ) than from iNOS ( $k_{\text{off}} = 0.005 \text{ min}^{-1}$ ) in the absence of L-Arg (50, 51). In solution, free BH4 degrades with a half-life of 16 min to 7,8-dihydrobiopterin and 7,8-dihydropterin (52, 53). Therefore, during crystallization, BH4 largely remains bound to iNOS<sub>ox</sub>, but exchanges rapidly between eNOS<sub>ox</sub> and solution, where it is more susceptible to degradation. These differences in BH4 binding to the structurally similar pterin-binding sites

of NOS isozymes are reflected not only in our crystal structures but also in NOS dimer stability (54).

NOS requires BH4 for normal activity, and furthermore, in vivo eNOS<sub>ox</sub> may function in environments where BH4 is limiting (55, 56). Thus, the finding that 3Br7NI binds in the eNOS<sub>ox</sub> BH4 binding site may be important in designing therapeutics. Desirable isozyme-specific inhibitors should have low affinity not only for the eNOS<sub>ox</sub> active site but also for the pterin-binding site.

*Pterin Tethers the Heme Carboxylate in iNOS<sub>ox</sub> and Influences Inhibitor Binding.* In substrate-bound NOS<sub>ox</sub>, L-Arg hydrogen bonds not only through its side chain guanidinium group to the carbonyl of Trp366 and bidentate to Glu371 but also through its main chain nitrogen to heme propionate A (10). Heme propionate A also hydrogen bonds to BH4, both directly with pterin N3 and indirectly through a water molecule to pterin O4. In structures of NOS<sub>ox</sub>–inhibitor complexes reported here, the conformational changes in Glu371 (and the absence of L-Arg) disrupt this hydrogen bonding network, but, in contrast to previous reports (24), need not produce conformational changes in the heme carboxylate. Movements in the heme propionate occur in eNOS<sub>ox</sub> complexes, where BH4 is dissociated from the pterin site, but not in iNOS<sub>ox</sub> complexes, where BH4 remains bound and tethered to heme propionate A.

Isozyme differences in BH4 cofactor occupancy and flexibility of the heme propionate may influence inhibitor binding, as can be seen by comparing iNOS<sub>ox</sub> and eNOS<sub>ox</sub> complexes with the same inhibitors (Figure 2). In BH4-free eNOS<sub>ox</sub>, observed structural changes in heme propionate A allowed inhibitors to pack more tightly against the heme. For example, the inhibitor plane of 3Br7NI is tilted 20° up from the heme plane in iNOS<sub>ox</sub>, but rotation of heme propionate A in eNOS<sub>ox</sub> allows 3Br7NI to bind parallel to the heme plane.

*Implications for Isozyme-Selective NOS Inhibition.* CHLZ and nitroindazoles inhibit NOS through a molecular recognition mechanism based on an induced conformational change in the substrate-binding residue Glu371. Our crystallographic, computational, and biochemical results argue that  $\pi$ -stacking with the heme and hydrogen bonding to the Met368 amide nitrogen and Trp366 carbonyl oxygen contribute significantly to binding affinity. We estimate the energetic cost of inducing the conformational change in Glu371 to be  $\sim 1$ –2 kcal/mol. Compensating for this energetic barrier likely decreases inhibitor potency by one order of magnitude. To improve the efficacy of nitroindazoles, affinity and selectivity must be optimized. Potency could be enhanced by designing compounds that bind similarly to the nitroindazoles, but also interact with Glu371 in the inhibitor-induced position. Alternatively, compounds that stack as effectively as 7NI or CHLZ with the heme, without inducing the Glu371 conformational change, would likely bind more tightly.

While CHLZ, 7NI, and 3Br7NI have low in vitro isoform selectivity, 7NI is selective in vivo for nNOS (19). Nitroindazoles, therefore, because of their tissue distribution, may be a useful scaffold for further drug design. Conformational changes in heme propionate A of eNOS<sub>ox</sub> and displacement of BH4 from the eNOS<sub>ox</sub> BH4 binding site may be advantageous differences for designing compounds with selectivity over eNOS<sub>ox</sub>.

## ACKNOWLEDGMENT

We thank David Goodsell, Michel Sanner, and Ruth Huey for providing developmental versions of AutoDock and AutoDockTools, and also for their critical input about automated docking and analysis. We also thank Mika Aoyagi, Andrew Arvai, David Shin, and Joseph Bonaventura for insightful comments on this work. X-ray crystallographic data were collected at Stanford Synchrotron Radiation Laboratories (SSRL) and at the Advanced Light Source (ALS).

## REFERENCES

- Marletta, M. A. (1994) Nitric oxide synthase: aspects concerning structure and catalysis, *Cell* 78, 927–930.
- Griffith, O. W., and Stuehr, D. J. (1995) Nitric oxide synthases: properties and catalytic mechanism, *Annu. Rev. Physiol.* 57, 707–736.
- Masters, B. S., McMillan, K., Nishimura, J., Martasek, P., Roman, L. J., Sheta, E., Gross, S. S., and Salerno, J. (1996) Understanding the structural aspects of neuronal nitric oxide synthase (NOS) using microdissection by molecular cloning techniques: molecular dissection of neuronal NOS, *Adv. Exp. Med. Biol.* 387, 163–169.
- Ignarro, L. J. (1999) Nitric oxide: a unique endogenous signaling molecule in vascular biology, *Biosci. Rep.* 19, 51–71.
- Murad, F. (1999) Cellular signaling with nitric oxide and cyclic GMP, *Braz. J. Med. Biol. Res.* 32, 1317–1327.
- Dinerman, J. L., Lowenstein, C. J., and Snyder, S. H. (1993) Molecular mechanisms of nitric oxide regulation. Potential relevance to cardiovascular disease, *Circ. Res.* 73, 217–222.
- Schmidt, H. H., and Walter, U. (1994) NO at work, *Cell* 78, 919–925.
- Griffith, O. W., and Kilbourn, R. G. (1997) Design of nitric oxide synthase inhibitors and their use to reverse hypotension associated with cancer immunotherapy, *Adv. Enzyme Regul.* 37, 171–194.
- Fischmann, T. O., Hruza, A., Niu, X. D., Fossetta, J. D., Lunn, C. A., Dolphin, E., Prongay, A. J., Reichert, P., Lundell, D. J., Narula, S. K., and Weber, P. C. (1999) Structural characterization of nitric oxide synthase isoforms reveals striking active-site conservation, *Nat. Struct. Biol.* 6, 233–242.
- Crane, B. R., Arvai, A. S., Ghosh, D. K., Wu, C., Getzoff, E. D., Stuehr, D. J., and Tainer, J. A. (1998) Structure of nitric oxide synthase oxygenase dimer with pterin and substrate, *Science* 279, 2121–2126.
- Raman, C. S., Li, H., Martasek, P., Kral, V., Masters, B. S., and Poulos, T. L. (1998) Crystal structure of constitutive endothelial nitric oxide synthase: a paradigm for pterin function involving a novel metal center, *Cell* 95, 939–950.
- Crane, B. R., Arvai, A. S., Gachhui, R., Wu, C., Ghosh, D. K., Getzoff, E. D., Stuehr, D. J., and Tainer, J. A. (1997) The structure of nitric oxide synthase oxygenase domain and inhibitor complexes, *Science* 278, 425–431.
- Gachhui, R., Ghosh, D. K., Wu, C., Parkinson, J., Crane, B. R., and Stuehr, D. J. (1997) Mutagenesis of acidic residues in the oxygenase domain of inducible nitric-oxide synthase identifies a glutamate involved in arginine binding, *Biochemistry* 36, 5097–5103.
- Chen, P. F., Tsai, A. L., Berka, V., and Wu, K. K. (1997) Mutation of Glu-361 in human endothelial nitric-oxide synthase selectively abolishes L-arginine binding without perturbing the behavior of heme and other redox centers, *J. Biol. Chem.* 272, 6114–6118.
- Crane, B. R., Arvai, A. S., Ghosh, S., Getzoff, E. D., Stuehr, D. J., and Tainer, J. A. (2000) Structures of the  $\omega$ -hydroxy-L-arginine complex of inducible nitric oxide synthase oxygenase dimer with active and inactive pterins, *Biochemistry* 39, 4608–4621.
- Babu, B., Frey, C., and Griffith, O. (1999) L-Arginine binding to nitric oxide synthase: The role of H-bonds to the nonreactive guanidinium nitrogens, *J. Biol. Chem.* 274, 25218–25226.
- Li, H., Raman, C. S., Martasek, P., Kral, V., Masters, B. S., and Poulos, T. L. (2000) Mapping the active site polarity in structures of endothelial nitric oxide synthase heme domain complexed with isothioureas, *J. Inorg. Biochem.* 81, 133–139.
- Babu, B. R., and Griffith, O. W. (1998) Design of isoform-selective inhibitors of nitric oxide synthase, *Curr. Opin. Chem. Biol.* 2, 491–500.
- Southan, G. J., and Szabo, C. (1996) Selective pharmacological inhibition of distinct nitric oxide synthase isoforms, *Biochem. Pharmacol.* 51, 383–394.
- Moore, P. K., Babbedge, R. C., Wallace, P., Gaffen, Z. A., and Hart, S. L. (1993) 7-Nitro indazole, an inhibitor of nitric oxide synthase, exhibits anti-nociceptive activity in the mouse without increasing blood pressure, *Br. J. Pharmacol.* 108, 296–297.
- Grant, S. K., Green, B. G., Wang, R., Pacholok, S. G., and Kozarich, J. W. (1997) Characterization of inducible nitric-oxide synthase by cytochrome P-450 substrates and inhibitors. Inhibition by chlorzoxazone, *J. Biol. Chem.* 272, 977–983.
- Peter, R., Bocker, R., Beaune, P. H., Iwasaki, M., Guengerich, F. P., and Yang, C. S. (1990) Hydroxylation of chlorzoxazone as a specific probe for human liver cytochrome P-450IIE1, *Chem. Res. Toxicol.* 3, 566–573.
- Kharasch, E. D., Thummel, K. E., Mhyre, J., and Lillibridge, J. H. (1993) Single-dose disulfiram inhibition of chlorzoxazone metabolism: a clinical probe for P450 2E1, *Clin. Pharmacol. Ther.* 53, 643–650.
- Raman, C. S., Li, H., Martasek, P., Southan, G., Masters, B. S., and Poulos, T. L. (2001) Crystal structure of Nitric Oxide Synthase Bound to Nitro Indazole Reveals a Novel Inactivation Mechanism, *Biochemistry* 40, 13448–13455.
- Rosenfeld, R. J., Garcin, E., Olson, A., Tainer, J. A., and Getzoff, E. D. (2000) in *First International Conference: Biology, Chemistry, and Therapeutic Applications of Nitric Oxide* (Parkinson, J. F., and Rubanyi, G. M., Eds.) pp 201, Academic Press, San Francisco.
- Raman, C. S., Li, H., Martasek, P., Southan, G., Poulos, T. L., and Masters, B. S. (2000) in *First International Conference: Biology, Chemistry, and Therapeutic Applications of Nitric Oxide* (Parkinson, J. F., and Rubanyi, G. M., Eds.) Academic Press, San Francisco (Addendum).
- Ghosh, D. K., Wu, C., Pitters, E., Moloney, M., Werner, E. R., Mayer, B., and Stuehr, D. J. (1997) Characterization of the inducible nitric oxide synthase oxygenase domain identifies a 49 amino acid segment required for subunit dimerization and tetrahydrobiopterin interaction, *Biochemistry* 36, 10609–10619.
- Otwinowski, Z., and Minor, W. (1997) Processing of X-ray diffraction data collected in oscillation mode, *Methods Enzymol.* 276, 307–336.
- Brunker, A., Adams, P., Clore, G., DeLano, W., Gros, P., Grosse-Kunstleve, W., Jiang, J.-S., Kuszewski, J., Nilges, M., Pannu, N., Read, R., Rice, L., Simonson, T., and Warren, G. (1998) *Crystallography & NMR System: A New Software Suite for Macromolecular Structure Determination*, *Acta Crystallogr. D54*, 905–921.
- McRee, D. (1999) XtalView/Xfit: A versatile program for manipulating atomic coordinates and electron density, *J. Struct. Biol.* 125, 156–165.
- Adak, S., Ghosh, S., Abu-Soud, H. M., and Stuehr, D. J. (1999) Role of reductase domain cluster 1 acidic residues in neuronal nitric-oxide synthase. Characterization of the FMN-free enzyme, *J. Biol. Chem.* 274, 22313–22320.
- Wu, C., Zhang, J., Abu-Soud, H., Ghosh, D. K., and Stuehr, D. J. (1996) High-level expression of mouse inducible nitric oxide synthase in *Escherichia coli* requires coexpression with calmodulin, *Biochem. Biophys. Res. Commun.* 222, 439–444.
- Matsuoka, A., Stuehr, D. J., Olson, J. S., Clark, P., and Ikeda-Saito, M. (1994) L-Arginine and calmodulin regulation of the heme iron reactivity in neuronal nitric oxide synthase, *J. Biol. Chem.* 269, 20335–20339.
- Cheng, Y., and Prusoff, W. (1973) Relationship between the inhibition constant ( $K_i$ ) and the concentration of inhibitor which causes 50% inhibition ( $IC_{50}$ ) of an enzymatic reaction, *Biochem. Pharmacol.* 22, 3099–3108.
- Singh, U. C., and Kollman, P. A. (1984) An approach to computing electrostatic charges for molecules, *J. Comput. Chem.* 5, 145–159.
- Bessler, B. H., Merz, K. M., Jr., and Kollman, P. A. (1990) Atomic charges derived from semiempirical methods, *J. Comput. Chem.* 11, 431–439.
- Morris, G. M., Goodsell, D. S., Halliday, S., Huey, R., Hart, W. E., Belew, R. K., and Olson, A. J. (1998) AutoDock 3.0:

- Automated Docking using a Lamarckian Genetic Algorithm and an Empirical Free Energy Function, *J. Comput. Chem.* **19**, 1639–1662.
38. Sanner, M. F., Duncan, B. S., Carrillo, C. J., and Olson, A. J. (1999) in *Biocomputing '99: Proceedings of the Pacific Symposium* (Altman, R. B., Lauderdale, K., Dunker, A. K., Hunter, L., and Klein, T. E., Eds.) pp 401–412, World Scientific Press, Mauna Lani, HI.
39. Sopkova-de Oliveira Santos, J., Collot, V., and Rault, S. (2000) 7-Nitro-1H-indazole, an inhibitor of nitric oxide synthase, *Acta Crystallogr. C* **56**, 1503–1504.
40. Zinner, L. B., Ayala, J. D., Andrade de Silva, M. A., Bombieri, G., and Del Pra, A. (1994) Synthesis, characterization, and structure of lanthanide picrate complexes with tetramethylene-sulfoxide (TMSO), *J. Chem. Crystallogr.* **24**, 445–450.
41. Moore, P. K., and Bland-Ward, P. A. (1996) 7-Nitroindazole: an inhibitor of nitric oxide synthase, *Methods Enzymol.* **268**, 393–398.
42. Hunter, C. A., and Sanders, J. K. M. (1990) The nature of pi-pi interactions, *J. Am. Chem. Soc.* **112**, 5525–5534.
43. Janiak, C. (2000) A critical account on pi-pi stacking in metal complexes with aromatic nitrogen-containing ligands, *J. Chem. Soc., Dalton Trans.*, 3885–3869.
44. Jorgensen, W. L., and Severance, D. L. (1990) Aromatic–Aromatic Interactions: Free Energy Profiles for the Benzene Dimer in Water, Chloroform, and Liquid Benzene, *J. Am. Chem. Soc.* **112**, 4768–4774.
45. Kharasch, E. D., and Thummel, K. E. (1993) Identification of cytochrome P450 2E1 as the predominant enzyme catalyzing human liver microsomal defluorination of sevoflurane, isoflurane, and methoxyflurane, *Anesthesiology* **79**, 795–807.
46. Najmanovich, R., Kutter, J., Sobolev, V., and Edelman, M. (2000) Side-chain flexibility in proteins upon ligand binding, *Proteins: Struct., Funct., Genet.* **39**, 261–268.
47. Crane, B. R., Rosenfeld, R. J., Arvai, A. S., Ghosh, D. K., Ghosh, S., Tainer, J. A., Stuehr, D. J., and Getzoff, E. D. (1999) N-Terminal domain swapping and metal ion binding in nitric oxide synthase dimerization, *EMBO J.* **18**, 6271–6281.
48. Aoyagi, M., Arvai, A. S., Ghosh, S., Stuehr, D. J., Tainer, J. A., and Getzoff, E. D. (2001) Structures of tetrahydrobiopterin binding-site mutants of inducible nitric oxide synthase dimer and implicated roles of Trp457, *Biochemistry* **40**, 12826–12832.
49. Li, H., Raman, C. S., Glaser, C. B., Blasko, E., Young, T. A., Parkinson, J. F., Whitlow, M., and Poulos, T. L. (1999) Crystal structures of zinc-free and -bound heme domain of human inducible nitric-oxide synthase. Implications for dimer stability and comparison with endothelial nitric-oxide synthase, *J. Biol. Chem.* **274**, 21276–21284.
50. List, B. M., Klosch, B., Volker, C., Gorren, A. C., Sessa, W. C., Werner, E. R., Kukovetz, W. R., Schmidt, K., and Mayer, B. (1997) Characterization of bovine endothelial nitric oxide synthase as a homodimer with downregulated uncoupled NADPH oxidase activity: tetrahydrobiopterin binding kinetics and role of haem in dimerization, *Biochem. J.* **323**, 159–165.
51. Mayer, B., Wu, C., Gorren, A. C., Pfeiffer, S., Schmidt, K., Clark, P., Stuehr, D. J., and Werner, E. R. (1997) Tetrahydrobiopterin binding to macrophage inducible nitric oxide synthase: heme spin shift and dimer stabilization by the potent pterin antagonist 4-amino-tetrahydrobiopterin, *Biochemistry* **36**, 8422–8427.
52. Stone, K. J. (1976) The role of tetrahydrofolate dehydrogenase in the hepatic supply of tetrahydrobiopterin in rats, *Biochem. J.* **157**, 105–109.
53. Kaufman, S. (1967) Metabolism of the phenylalanine hydroxylation cofactor, *J. Biol. Chem.* **242**, 3934–3943.
54. Panda, K., Rosenfeld, R. J., Ghosh, S., Meade, A. L., Getzoff, E. D., and Stuehr, D. J. (2002) Distinct Dimer Interaction and Regulation in Nitric Oxide Synthase Types I, II, and III, *J. Biol. Chem.* **277**, 31020–31030.
55. Cosentino, F., and Luscher, T. F. (1998) Tetrahydrobiopterin and endothelial function, *Eur. Heart J.* **19**, G3–G8.
56. Werner, E. R., Werner-Felmayer, G., Wachter, H., and Mayer, B. (1995) Biosynthesis of nitric oxide: dependence on pteridine metabolism, *Rev. Physiol. Biochem. Pharmacol.* **127**, 97–135.

BI026313J